J Mater Sci: Mater Electron (2017) 28:493–500
DOI 10.1007/s10854-016-5548-4

CrossMark

The structural, optical, ferroelectric properties of (1-x)$BiFeO_3$-$x$$CaTiO_3$ thin films by a sol–gel method

Xiaohang Wu[1] · Daihong Kuang[1,2] · Lu Yao[1] · Shenghong Yang[1] · Yueli Zhang[1]

Received: 11 June 2016 / Accepted: 11 August 2016 / Published online: 16 August 2016
© Springer Science+Business Media New York 2016

Abstract (1-x)$BiFeO_3$-$x$$CaTiO_3$ ((1-x)BFO-xCTO, $x = 0$, 0.05, 0.10, 0.15, 0.20) thin films were successfully grown on Pt(111)/Ti/SiO_2/Si(100) substrates using a sol–gel spin coating method. The structure stabilities of BFO thin films were improved by introducing CTO due to the increase of their tolerance factor. The X-ray diffraction patterns indicated that all the samples had a single perovskite structure. The merging phenomenon of (110) and (104) diffraction peaks demonstrated a distortion of the lattice structure in BFO thin films by introducing CTO. The atomic force microscope showed all the samples had dense, crack-free and uniform morphology. The leakage current density decreased with the increasing of CTO contents. At the applied electric field of 300 kV/cm, the leakage current density of the 0.85BFO-0.15CTO was 1.42×10^{-8} A/cm^2, which is about 4 orders of magnitude lower than that of the pure BFO thin film (5.78×10^{-4} A/cm^2). The leakage conduction mechanism showed Ohmic conduction for all thin films in the low electric field region. In the high electric field region, the leakage mechanisms were dominated by the space-charge-limited current behavior for 0.80BFO-0.20CTO and the Fowler-Norheim tunneling for (1-x)BFO-xCTO ($x = 0.10$, 0.15) thin films. The remnant polarization ($2P_r$) and spontaneous polarization (P_s) of (1-x)BFO-xCTO ($x = 0.10$, 0.15, 0.20) were obviously improved. The 0.85BFO-0.15CTO thin film showed the best ferroelectricity with large remnant polarization of 39.88 μC/cm^2 while the remnant polarization of the pure BFO was 3.74 μC/cm^2 at the electric field of 300 kV/cm. The absorption edges of (1-x)BFO-xCTO thin films are blue-shift with the increasing of x value. The structural, optical properties and ferroelectricity of BFO thin films were improved by introducing CTO.

✉ Yueli Zhang
stszyl@mail.sysu.edu.cn

[1] State Key Laboratory of Optoelectronic Materials and Technologies, School of Materials Science and Engineering/ School of Physics, Sun Yat-Sen University, Guangzhou 510275, China

[2] School of Mathematics and Physics, Xinjiang Agricultural University, Urumqi 830052, China

1 Introduction

Multiferroic materials are well-known, which simultaneously have two or more properties of ferromagnetism, ferroelectricity and ferroelasticity [1–4]. It attracts enormous attention because of its potential applications, such as information storage, spintronic devices and sensors [4, 5]. $BiFeO_3$ (BFO) is the most promising room-temperature multiferroic material with high Curie ($T_C \sim 1103$ K) and Neel temperature ($T_N \sim 643$ K) [4]. BFO has a rhombohedral distorted perovskite structure with space group R3c. The origin of ferroelectricity is ascribed to the stereochemically active Bi 6 s^2 lone pair electron, while the weak ferromagnetism originates from the residual moment of the Fe^{3+} spin structure [6, 7]. The large leakage current, poor ferroelectric hysteresis loops and weak ferromagnetism hinder the application of BFO. In order to overcome the shortage of BFO, the effective methods including the improved process of fabricating BFO thin film [8–10], doping/co-doping [11–13], BFO-ABO_3 bilayered structure [14, 15] and solid-solutions [16–18], were reported. BFO-ABO_3 solid-solutions become more interesting, because it can enhance the multiferroic properties of BFO. But most of the studies were about ceramic materials [19, 20]. Singh et al. [5] reported BFO-$BaTiO_3$ ceramics have some impacts on the ferromagnetism and explained the origin of

weak ferromagnetism in terms of the Dzyaloshinskii-Moriya interaction and dilution effects of the Fe^{3+} sublattice. Lahmar et al. [21] investigated the interplay of BFO-$LaMnO_3$ solid solution thin films. The addition of $LaMnO_3$ to BFO thin films induced the structural change, reduced the leakage currents and improved the ferroelectric properties. Also, the correlations between distortion, leakage current and polarization properties were found. The smaller leakage current and the higher polarization were obtained at the higher distortion. Mutiferroic BFO-$PbTiO_3$ thin films have been studied [22, 23], which exhibit the low dielectric loss, the weak ferromagnetism and the slim ferroelectric hysteresis loops. Liu et al. [24] reported that both ferroelectric (P_r = 12.5 μC/cm^2) and magnetic properties are significantly improved in $(Sr_{0.5}Ca_{0.5})TiO_3$-BFO ceramics. The improvement of ferroelectricity is mainly due to the suppressed leakage current, and the enhanced magnetism originates from the destruction of previous spiral structure for the partial substitution of Fe^{3+} by Ti^{4+} ions. Wang et al. [25] reported that the BFO-$CaTiO_3$ (CTO) ceramics could improve its structure stability and multiferroic characteristics with the increased dielectric constant, the improved ferroelectricity and the enhanced remnant magnetization. A remnant polarization of 0.28 μC/cm^2 was found in the 0.80BFO-0.20CTO solid-solution ceramic. Although the enhanced ferroelectric properties of BFO-CTO solid solutions have been reported, the polarization is still not high. Moreover, as far as we know, the effects of CTO on optical characteristics and the leakage mechanisms of BFO-CTO thin films have not been reported. For fabricating BFO-CTO solid solutions, several methods have been reported such as solid state reaction, chemical solution deposition and so on [21, 25, 26]. Comparing with other methods, sol–gel spin coating technique is the candidate method for preparing BFO-CTO thin films due to uniform thickness, simplest and cost effective [15]. Therefore the better improvement in ferroelectric properties and lower leakage current of BFO-CTO thin films can be expected by a sol–gel method. The optical properties and the leakage mechanisms of BFO-CTO thin films are studied in this paper.

In this work, BFO modified by introducing CTO with different content were prepared on Pt(111)/Ti/SiO_2/Si(100) substrates using a sol–gel method. The structural, ferroelectric and optical properties of (1-x)BFO-xCTO (x = 0, 0.05, 0.1, 0.15, 0.2) thin films were investigated and the leakage mechanisms were discussed in detail.

2 Experimental details

(1-x)BFO-xCTO (x = 0, 0.05, 0.1, 0.15, 0.2) thin films were grown on Pt(111)/Ti/SiO_2/Si(100) substrates by the sol–gel spin coating method. Bismuth nitrate pentahydrate ($Bi(NO_3)_3.5H_2O$), iron nitrate nonahydrate ($Fe(NO_3)_3.9H_2O$), calcium nitrate tetrahydrate ($Ca(NO_3)_2.4H_2O$), tetrabutyl titanate ($[CH_3(CH_2)_3O]_4Ti$) as the raw materials were used to synthesize the precursor solutions. $Bi(NO_3)_3.5H_2O$ (excess 5 % to compensate the Bi loss) and $Fe(NO_3)_3.9H_2O$ were dissolved in 2-methoxyethanol and ethylene glycol mixture. After stirring for an hour, a small amount of acetic anhydride was added into the solutions to form the pure BFO precursor solutions. Finally, the proper ratios of $Ca(NO_3)_2.4H_2O$ and $[CH_3(CH_2)_3O]_4Ti$ were added to acquire the (1-x)BFO-xCTO (x = 0, 0.05, 0.1, 0.15, 0.2) precursor solutions. Then the solutions were stirred continuously for 2 h. The final concentration of the solutions was 0.25 mol/L.

The precursor solutions were spin-coated on the Pt(111)/Ti/SiO_2/Si(100) substrates. Each layer was deposited at 3000 rpm for 30 s and prefired at 350 °C for 10 min. This process was repeated for several times to obtain the desired thickness. Then, the films were carried out by a rapid thermal processor at 550 °C for 15 min.

The structure of (1-x)BFO-xCTO films was identified by X-ray diffractometer (XRD, D-MAX 2200 VPC, RIGAKU) with Cu $K\alpha$ radiation (λ = 0.154 nm). The microstructure and surface roughness characterization were carried out by using atomic force microscope (AFM; BRUKE Dimension fastscan). The thickness of thin film was measured by thermal FE environment scanning electron microscope (SEM, Quanta 400, Dutch Philips).The ferroelectric properties and leakage current density of all films were obtained using a ferroelectric test system (Precision Premier II, Radiant). The optical properties were measured using transmittance spectra (UV/vis Lambda 2S, Perkin- Elmer).

3 Results and discussion

Figure 1a displayed the XRD patterns of (1-x)BFO-xCTO (x = 0, 0.05, 0.1, 0.15, 0.2) thin films in the range of 2θ from 20° to 60°. The detectable diffraction peaks matched well with the distorted perovskite-type rhombohedral structure for the pure BFO thin film. No impurity phase was observed in all samples. Figure 1b shows that the (110) and (104) diffraction peaks of (1-x)BFO-xCTO (x = 0.05, 0.1, 0.15, 0.2) were merged into one peak in the vicinity of 32° compared with that of BFO, which inferred that the structure of (1-x)BFO-xCTO (x = 0.05, 0.1, 0.15, 0.2) transformed from rhombohedral to orthorhombic structure [12, 27]. The merged peaks move to the larger angles with increasing CTO content, which reveals the lattice constants decrease according to the Bragg equation. This can be attributed to the substitution of Bi^{3+} (0.103 nm) for Ca^{2+} (0.099 nm) and Fe^{3+} (0.0645 nm) for

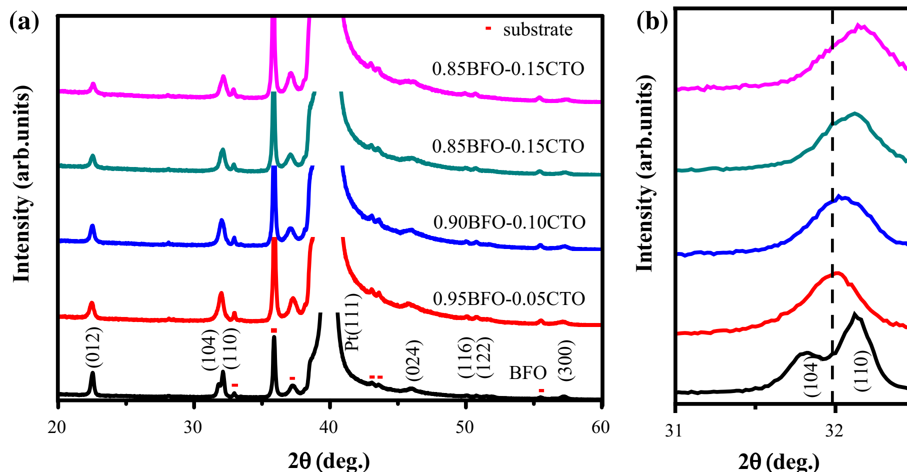

Fig. 1 **a** The XRD patterns of (1-x)BFO-xCTO thin films and **b** the enlarged XRD patterns from 31° to 32.5°

Ti^{4+} (0.0605 nm). For ABO_3-type perovskite structure, the Goldschmidt tolerance factor (t) can be calculated by [28]

$$t = \frac{R_A + R_O}{\sqrt{2}(R_B + R_O)}, \quad (1)$$

The R_A, R_B and R_O are the ionic radius of A, B and O, respectively. The tolerance factor are 0.84229, 0.84232, 0.84235, 0.84237, 0.84240 for (1-x)BFO-xCTO ($x = 0$, 0.05, 0.10, 0.15, 0.20) thin films, respectively. Therefore, the structural stabilities of (1-x) BFO-xCTO thin films were improved.

Figure 2a–e show the AFM images of (1-x)BFO-xCTO ($x = 0$, 0.05, 0.10, 0.15, 0.20) thin films in an area of $1.0 \times 1.0\ \mu m^2$. All the samples have dense, crack-free and uniform morphology. The root-mean-square (RMS) surface roughness values of the (1-x)BFO-xCTO thin films with $x = 0$, 0.05, 0.10, 0.15, 0.20 are 6.56, 3.31, 2.92, 2.43, 3.00 nm, and the average grain size are 110.07, 81.71, 67.89, 71.48, 85.48 nm, respectively. Compared with pure BFO, it's obvious that the surface roughness and the average grain size decrease with increasing CTO content. Figure 2f shows the cross section SEM images of pure BFO. As shown in Fig. 2f, the thickness of thin film is about 300 nm.

Figure 3 shows the plot of leakage current density (J) versus applied electric field (E) for (1-x)BFO-xCTO ($x = 0$, 0.05, 0.10, 0.15, 0.20) thin films. All the J-E curves exhibit good symmetry at negative and positive biases. At the applied electric field of 300 kV/cm, the leakage current density of (1-x)BFO-xCTO ($x = 0$, 0.05, 0.10, 0.15, 0.20) thin films are 5.78×10^{-4}, 1.75×10^{-4}, 5.21×10^{-8}, 1.42×10^{-8} and 5.56×10^{-5} A/cm^2, respectively. The leakage current density decreases with increasing the CTO contents except the 0.80BFO-0.20CTO. The leakage current density of 0.85BFO-0.15CTO thin film is the lowest, which is about 4 orders of magnitude lower than that of pure BFO thin film. According to the morphology of the samples, the surface roughness and the average grain size decrease with increasing CTO content. The reduction of the oxygen vacancies lead to the decrease of the leakage current, which results from that the bond energy of Ca-O is larger than that of Bi-O when the Ca ions substitute for A site [26], and the Ti ions substitute for B site could prevent the change of valence state of Fe ions [29].

Figure 4 illustrates the room temperature P-E hysteresis loops of (1-x)BFO-xCTO thin films measured at the electric field of 9 V. As shown in Fig. 4, the well-defined P-E hysteresis loops are obtained for all the thin films. The values of remnant polarization ($2P_r$) and spontaneous polarization (P_s) are shown in Table 1. It's obviously seen that the $2P_r$ and P_s of the samples increase and reach the maximum ($x = 0.15$) and then decrease with the increasing content of CTO. The $2P_r$ and P_s of 0.85BFO-0.15CTO are 39.88 and 49.27 μC/cm^2, while that of pure BFO are 3.74 and 7.86 μC/cm^2. Compared with the pure BFO, the $2P_r$ and P_s of 0.85BFO-0.15CTO approximately enhance ten times. This can be attributed to the reduction of leakage current density for BFO modified by introducing CTO. The ferroelectric property of BFO is originated from Bi 6s^2 lone pair [30]. Wang et al. [6] found that the Ti doped BFO improved the remnant polarization because of stabilizing the ferroelectric distortion rather than influencing the origin of ferroelectricity. Kim et al. [26] reported that 0.7$BiFeO_3$-0.3$CaTiO_3$ thin film would improve the ferroelectricity due to the lattice distortion. So BFO modified by CTO could not make apparent effects on the origin of ferroelectricity. The enhancement of ferroeletricity for (1-x)BFO-xCTO samples is ascribed to the more stable ferroelectric distortion and reduction of oxygen vacancies. What's more, the grain size of a sample may affect the polarization. It can be explained by the grain boundary, which is the weak ferroelectric region. The value of polarization may decrease as the grain size becomes smaller [29].

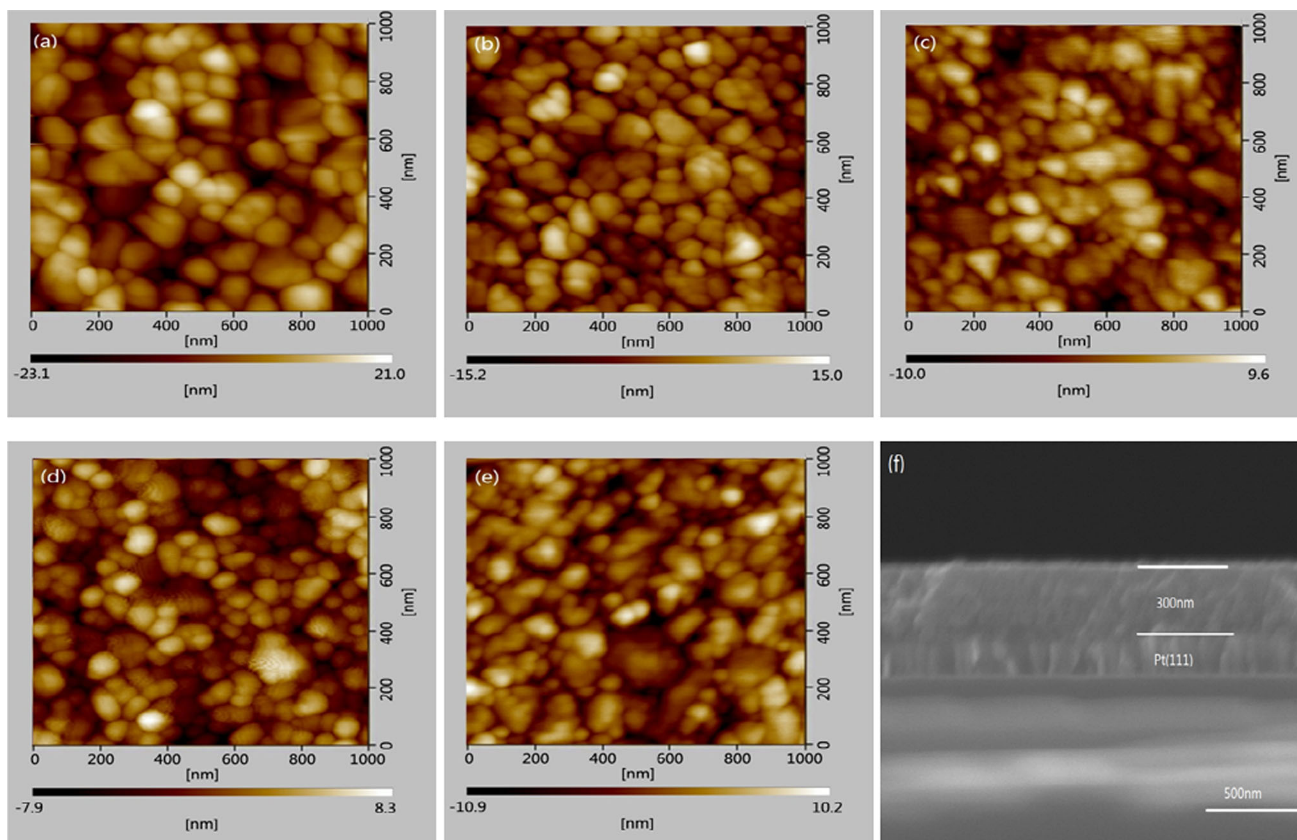

Fig. 2 **a–e** The AFM images of (1-x)BFO-xCTO (x = 0, 0.05, 0.10, 0.15, 0.20) thin films, and **f** the cross-section SEM image of BFO thin film

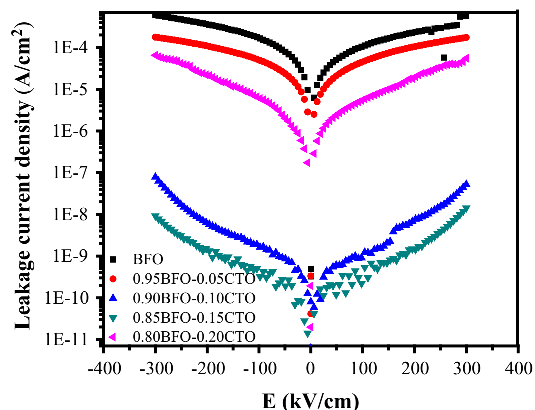

Fig. 3 The leakage current densities of (1-x)BFO-xCTO thin films

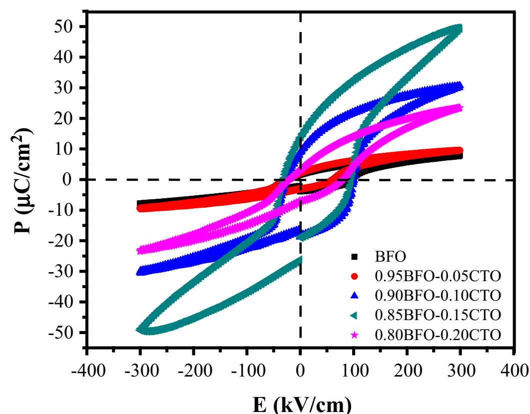

Fig. 4 Room temperature ferroelectric hysteresis loops of (1-x)BFO-xCTO thin films measured at ±300 kV/cm

There are many different leakage mechanisms, which were widely used to investigate the J-E characteristics of BFO thin films. The possible conduction mechanisms include Ohmic conduction, the Schottky emission (SE), the Fowler-Norheim (FN) tunneling, the space-charge-limited current (SCLC) and the Poole–Frenkel (PF) emission. The SE and FN tunneling are interface-limited conduction, whereas the SCLC and PF emission are bulk-limited conduction [31–33].

Table 1 The values of P_s and $2P_r$ of the (1-x)BFO-xCTO thin films

CTO content (at.%)	0	5 %	10 %	15 %	20 %
P_s (μC/cm^2)	7.86	9.52	30.67	49.27	23.48
$2P_r$ (μC/cm^2)	3.74	4.77	26.19	39.88	10.77

The Ohmic conduction is expressed by [29, 33]

$$J_O = ne\mu E, \tag{2}$$

$$\log J_O = \log E + \log(ne\mu), \tag{3}$$

where e is the electronic charge, n is the number of charge carriers, and μ is the carrier mobility and E is electric field. The slop value of log J versus log E is around 1, indicating that the dominant leakage mechanism is Ohmic conduction.

The SCLC can be expressed as [29, 31]

$$J_{SCLC} = \frac{9\mu\varepsilon_0\varepsilon_r E^2}{8d}, \tag{4}$$

$$\log J_{SCLC} = 2\log E + \log\frac{9\mu\varepsilon_0\varepsilon_r^2}{8d}, \tag{5}$$

where μ is the carrier mobility and E is electric field, ε_0 is the permittivity of free space, and ε_r is relative dielectric constant of films, and d is the film thickness. The slop value of log J versus log E is around 2, indicating that the dominant leakage mechanism is SCLC. The linear relationship of log J versus log E at a positive bias is shown in Fig. 5a. The slopes of (1-x)BFO-xCTO (x = 0, 0.05, 0.10, 0.15, 0.20) thin films at lower electric field are 1.06, 1.12, 1.09, 1.17 and 1.14, respectively. It suggests that the conduction behavior is Ohmic conduction. The slope value of 0.80BFO-0.20CTO thin film is 2.36 in the electric field above 1.78 × 10^7 V/m, in agreement with SCLC behavior. While the slope values for (1-x)BFO-xCTO (x = 0.10, 0.15) are 3.93 and 4.54 in the electric field above 1.53 × 10^7 V/m. It suggests that there are discrete traps embedded in the background of continuously distributed traps in ferroelectric thin films, which will induce a vertical regime with infinite slope in log J versus log E plots [31]. There are no such regimes in the plots, so the traps should be continuously distributed.

The interfacial-limited SE arises from the energy difference in Fermi levels between a metal and a semiconductor where carrier transportation has to overcome the potential barrier, and it can be expressed by [32]

$$J_{SE} = AT^2 \exp\left[\frac{-(\phi_B - e\sqrt{eE/4\pi\varepsilon_0 K})}{k_B T}\right], \tag{6}$$

$$\ln\frac{J_{SE}}{T^2} = \sqrt{\frac{e^3}{k_B^2 T^2 \times 4\pi\varepsilon_0 K}}E^{\frac{1}{2}} - \frac{\phi_B}{k_B T} + \ln(A), \tag{7}$$

$$K = \frac{e^3}{k_B^2 T^2 \times 4\pi\varepsilon_0 \alpha^2}, \tag{8}$$

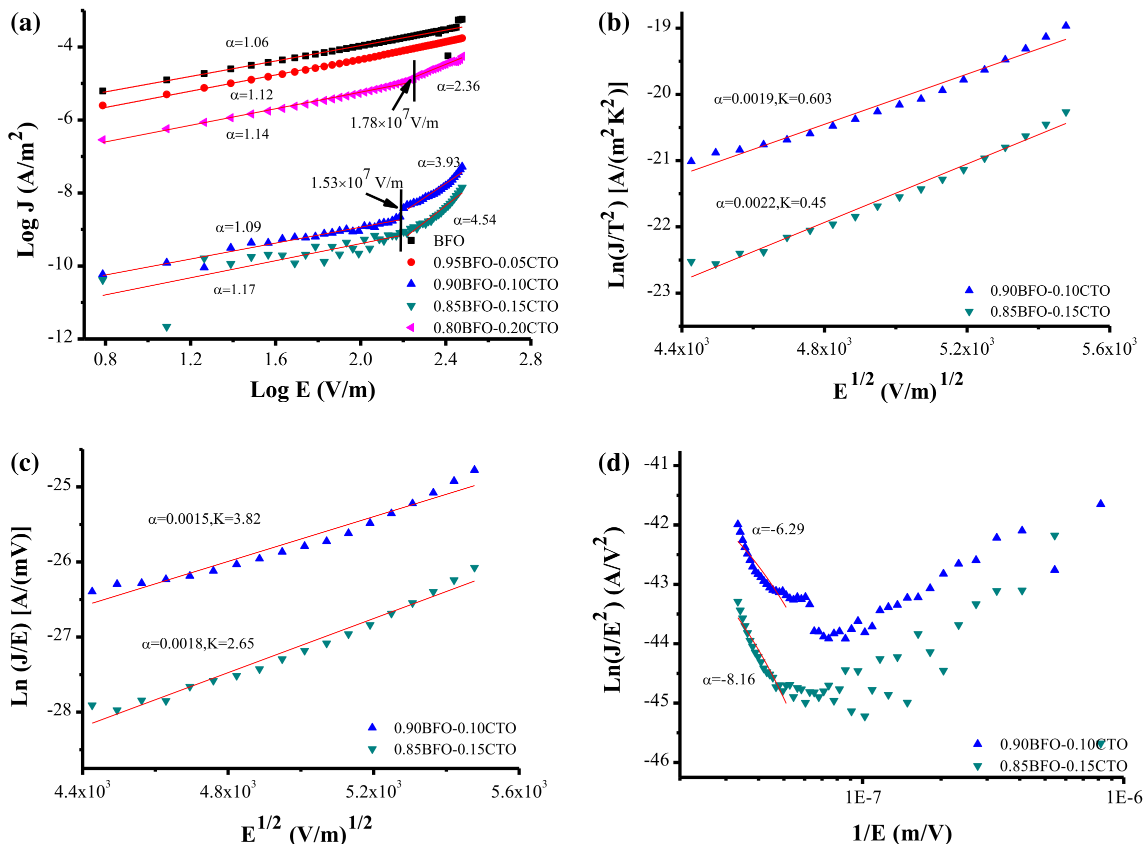

Fig. 5 The leakage current densities versus electric field characteristics of the (1-x)BFO-xCTO thin films. **a** Ohmic conduction and SCLC, **b** SE, **c** PF emission and **d** FN tunneling

where A is Richardson constant, φ_B is the Schottky barrier height, K is the optical dielectric constant, T is the temperature and k_B is Boltzmann constant. Figure 5b shows $\ln(J/T^2)$ versus $E^{1/2}$ plots of (1-x)BFO-xCTO ($x = 0.10$, 0.15) thin films at a positive bias. The refraction index (n) of BFO is 2.5, and the optical dielectric constant ($K = n^2$) is 6.25. The linear fittings are obtained, and the values of K calculated according to Eq. (5) for (1-x)BFO-xCTO ($x = 0.10$, 0.15) thin films are 0.603 and 0.45. These values are quite smaller than 6.25, suggesting there is no SE emission in the thin films.

The PF emission arises from the field-assisted thermal ionization of trapped carriers into the conduction band of thin films, and is described by [31, 32]

$$J_{PF} = AE\exp\left[\frac{-(\phi_i - e\sqrt{eE/\pi\varepsilon_0 K})}{k_B T}\right], \quad (9)$$

$$\ln\frac{J_{PF}}{E} = \sqrt{\frac{e^3}{k_B^2 T^2 \times \pi\varepsilon_0 K}}E^{\frac{1}{2}} - \frac{\phi_i}{k_B T} + \ln(A), \quad (10)$$

$$K = \frac{e^3}{k_B^2 T^2 \times \pi\varepsilon_0 \alpha^2}, \quad (11)$$

where A is constant, φ_i is the trap ionization energy, K is the optical dielectric constant, T is the temperature and k_B is Boltzmann constant. Figure 5c shows $\ln(J/E)$ versus $E^{1/2}$ curves of (1-x)BFO-xCTO ($x = 0.10$, 0.15) thin films at high electric field. The slope values can be obtained according to the linear fitting and K values of (1-x)BFO-xCTO ($x = 0.10$, 0.15) are 3.82 and 2.65 according to Eq. (7). The values are not close to 6.25, so the PF emission should be ruled out.

The FN tunneling is the effect that the injection of charge carriers into an insulator layer from electrodes may take place by tunneling through an interfacial energy barrier. It can be expressed as [32, 33]

$$J_{FN} = BE^2\exp\left(\frac{-C\phi_i^{\frac{3}{2}}}{E}\right), \quad (12)$$

$$\ln\frac{J_{FN}}{E^2} = -C\phi_i^{\frac{3}{2}}E^{-1} + \ln(B), \quad (13)$$

where B and C are constant, φ_i is the potential barrier height. Figure 5d shows the $\ln(J/E^2)$ versus $(1/E)$ at positive bias. The linear relation with the negative slope are obtained for (1-x)BFO-xCTO ($x = 0.10$, 0.15) thin films. At the high electric field, the leakage currents show the FN tunneling behavior. The FN tunneling mechanism demonstrates the formation of a partial depletion layer between thin film and the electrode.

The leakage conduction mechanism is dominated by Ohmic conduction for all thin films at the low electric field. The bulk-limited SCLC behavior is responsible for the conduction of 0.80BFO-0.20CTO in electric field above 1.78×10^7 V/m. Neither PF nor SE emission does exist in the thin films. And the leakage currents show FN tunneling for (1-x)BFO-xCTO ($x = 0.10$, 0.15) thin films at the high electric field above 1.53×10^7 V/m.

Figure 6a shows the UV–visible absorption spectra of (1-x)BFO-xCTO ($x = 0$, 0.05, 0.10, 0.15, 0.20) thin films. According to the Tauc's law [34], the relationship of absorption coefficient and energy can be described as $\alpha h\nu = A(h\nu - E_g)^{1/2}$, where A, h, ν, E_g, α are a constant, Plank constant, light frequency, optical band gap and absorption coefficient, respectively. The $(\alpha h\nu)^2$ versus $h\nu$ plots of all samples are shown in Fig. 6b, and the optical band gap (E_g) could be obtained from the tangent line of the plots [35]. E_g of (1-x)BFO-xCTO ($x = 0$, 0.05, 0.10, 0.15, 0.20) thin films are 2.34, 2.54, 2.59, 2.58, 2.60 eV, respectively. Obviously, a little blue shift of the optical band gap was presented when the CTO content increased because the E_g of CTO is $\sim$ 3.5 eV [36]. This

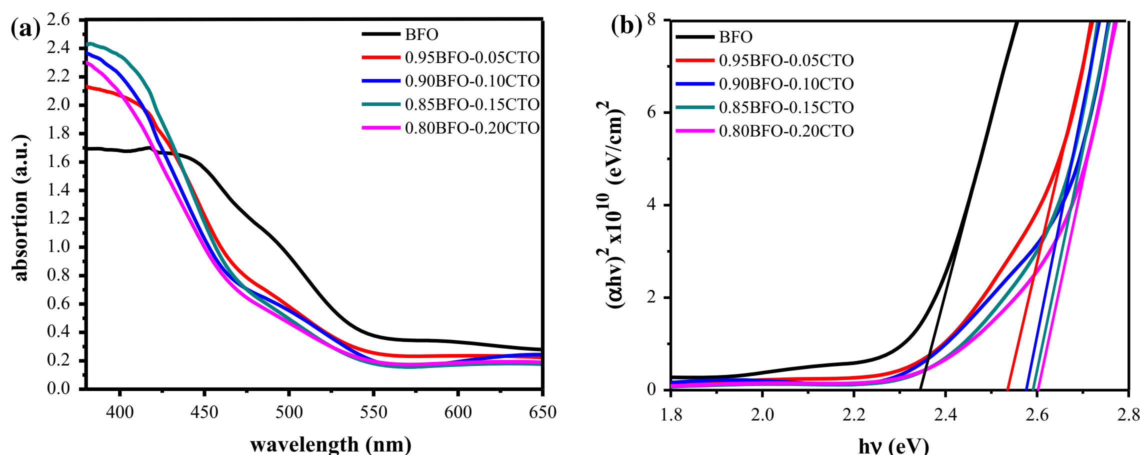

Fig. 6 **a** UV–visible absorption spectra and **b** the $(\alpha h\nu)^2$ versus $h\nu$ plots of (1-x)BFO-xCTO thin films

phenomenon was maybe caused by the Burstein-Moss effect [37, 38], which the Fermi energy lies inside conduction band, then E_g will increase due to Pauli's exclusion principle.

4 Conclusions

(1-x)BFO-xCTO ($x = 0$, 0.05, 0.10, 0.15, 0.20) thin films are successfully fabricated on the Pt(111)/Ti/SiO_2/Si(100) substrates by a sol–gel spin coating technique. The XRD indicates that all the samples had a single perovskite structure and BFO modified by introducing CTO have a structural distortion. The AFM images show all the samples had dense, crack-free and uniform morphology. The RMS values of the (1-x)BFO-xCTO thin films with $x = 0$, 0.05, 0.10, 0.15, 0.20 are 6.56, 3.31, 2.92, 2.43 and 3.00 nm, respectively. The average grain sizes are 110.07, 81.71, 67.89, 71.48 and 85.48 nm, respectively. The leakage current density decreases with increasing the CTO contents except 0.80BFO-0.20CTO. The 0.85BFO-0.15CTO has the lowest leakage current density (1.42×10^{-8} A/cm^2), which is about 4 orders of magnitude lower than that of the pure BFO thin film. The leakage behaviors show Ohmic conduction for all thin films in the low electric field region. The leakage mechanism is dominated by SCLC behavior for 0.80BFO-0.20CTO at high electric field ($>1.78 \times 10^7$ V/m), while FN tunneling is responsible for the conduction of (1-x)BFO-xCTO ($x = 0.10$, 0.15) thin films at high electric field ($>1.53 \times 10^7$ V/m). There are no PF and SE emission effects in the films. The $2P_r$ and P_s of the samples increase and reach the maximum ($x = 0.15$) and then decrease with the increasing content of CTO. The 2 P_r and P_s of (1-x)BFO-xCTO ($x = 0.10$, 0.15, 0.20) are enhanced. Compared with other samples, the 0.85BFO-0.15CTO thin film shows the best ferroelectric properties. The E_g of (1-x)BFO-xCTO thin films with $x = 0$, 0.05, 0.10, 0.15, 0.20 are 2.34, 2.54, 2.59, 2.58 and 2.60 eV, respectively. The blue shift of E_g occurs as x increased. In summary, the stability of structure and the ferroelectric properties of BFO were improved by introducing CTO.

Acknowledgments This work was supported by the National Natural Science Foundation of China under Grant Nos. 61176010 and 61172027, Guangdong Natural Science Foundation under Grant No. 2014A030311049.

References

1. E.C. Aguiar, M.A. Ramirez, J.A. Cortes, L.S. Rocha, E. Borsari, A.Z. Simões, Ceram. Int. **41**, 13126–13134 (2015)
2. W. Eerenstein, N.D. Mathur, J.F. Scott, Nature **442**, 759–765 (2006)
3. S.K. Singha, H. Ishiwara, J. Appl. Phys. **102**, 094109 (2007)
4. J. Wang, J.B. Neaton, H. Zheng, V. Nagarajan, S.B. Ogale, B. Liu, D. Viehland, V. Vaithyanathan, D.G. Schlom, U.V. Waghmare, N.A. Spaldin, K.M. Rabe, M. Wuttig, R. Ramesh, Science **299**, 1719–1722 (2003)
5. A. Singh, A. Senyshyn, H. Fuess, S.J. Kennedy, D. Pandey, Phys. Rev. B **89**, 024108 (2014)
6. Y. Wang, C.W. Nan, Appl. Phys. Lett. **89**, 052903 (2006)
7. J.Z. Huang, Y. Shen, M. Li, C.W. Nan, J. Appl. Phys. **110**, 094106 (2011)
8. J.S. Hwang, J.Y. Cho, S.Y. Park, Y.J. Yoo, P.S. Yoo, B.W. Lee, Y.P. Lee, Appl. Phys. Lett. **106**, 062902 (2015)
9. M.J. Chen, J.N. Ding, J.H. Qiu, N.Y. Yuan, Mater. Lett. **139**, 325–328 (2015)
10. S.V. Vijayasundaram, G. Suresh, R. Kanaga-durai, Appl. Phys. A **121**, 681–688 (2015)
11. J. Liu, H.M. Deng, X.Z. Zhai, T. Lin, X.J. Meng, Y.Y. Zhang, W.L. Zhou, P.X. Yang, J.H. Chu, Mater. Lett. **133**, 49–52 (2014)
12. C. Yang, J.S. Jiang, F.Z. Qian, D.M. Jiang, C.M. Wang, W.G. Zhang, J. Alloys Compd. **507**, 29–32 (2010)
13. W.L. Zhou, H.M. Deng, H.Y. Cao, J. He, J. Liu, P.X. Yang, J.H. Chu, Mater. Lett. **144**, 93–96 (2015)
14. J.X. Zhang, H.W. Zheng, Y.G. Zhang, G.L. Yuan, W.X. Gao, X.Y. Liu, G.S. Yin, Y.Z. Gu, W.F. Zhang, Mater. Lett. **156**, 98–100 (2015)
15. S. Sharma, M. Tomar, A. Kumar, N.K. Puri, V. Gupta, AIP Adv. **5**, 107216 (2015)
16. R.A.M. Gotardo, D.S.F. Viana, M. Olzon-Dionysio, S.D. Souza, D. Garcia, J.A. Eiras, M.F.S. Alves, L.F. Cótica, I.A. Santos, A.A. Coelho, J. Appl. Phys. **112**, 104112 (2012)
17. E. Venkata Ramana, A. Mahajan, M.P.F. Graca, A. Srinivas, M.A. Valente, J. Eur. Ceram. Soc. **34**, 4201–4211 (2014)
18. M. Kumar, S. Shankar, R.K. Kotnala, O. Parkash, J. Alloys Compd. **577**, 222–227 (2013)
19. J. Kimura, M.T. Chentir, T. Shimizu, H. Uchida, H. Funakubo, AIP Adv. **6**, 015304 (2016)
20. D.V. Karpinsky, I.O. Troyanchuk, V. Sikolenko, V. Efimov, A.L. Kholkin, J. Appl. Phys. **113**, 187218 (2013)
21. A. Lahmar, S. Habouti, C.H. Solterbeck, M. Es-Souni, B. Elouadi, J. Appl. Phys. **105**, 014111 (2009)
22. H.C. Yu, H.Y. Guo, W.M. Zhu, J. Zhuang, W. Ren, Z.G. Ye, Thin Solid Films **585**, 82–85 (2015)
23. H.M. Li, J.G. Zhu, J. Zhuang, Y. Hu, M.Z. Huai, Q.S. Yang, J. Sol-Gel, Sci. Technol. **75**, 353–359 (2015)
24. J. Liu, X.Q. Liu, X.M. Chen, J. Appl. Phys. **117**, 174101 (2015)
25. Q.Q. Wang, Z. Wang, X.Q. Liu, X.M. Chen, J. Am. Ceram. Soc. **95**(2), 670–675 (2012)
26. J.W. Kim, C.M. Raghavan, S.S. Kim, J. Sol Gel Sci. Technol. **76**, 693–698 (2015)
27. Y.J. Ren, X.H. Zhun, J.L. Zhu, J.G. Zhu, D.Q. Xiao, Ceram. Int. **41**, S234–S239 (2015)
28. M. Gowrishankar, D. Rajan Babu, P. Saravanan, Mater. Lett. **171**, 34–37 (2016)
29. W. Cai, C.L. Fu, R.L. Gao, W.H. Jiang, X.L. Deng, G. Chen, J. Alloys Compd. **617**, 240–246 (2014)
30. R. Seshadri, N.A. Hill, Chem. Mater. **13**, 2892–2899 (2001)
31. H. Yang, M. Jain, N.A. Suvorova, H. Zhou, H.M. Luo, D.M. Feldmann, P.C. Dowden, R.F. DePaula, S.R. Foltyn, Q.X. Jia, Appl. Phys. Lett. **91**, 072911 (2007)
32. D.H. Kuang, P. Tang, S.H. Yang, Y.L. Zhang, J. Sol Gel Sci. Technol. **73**, 410–416 (2015)
33. Z.H. Chen, L. He, F. Zhang, J. Jiang, J.W. Meng, B.Y. Zhao, A.Q. Jiang, J. Appl. Phys. **113**, 184106 (2013)
34. J. Tauc, R. Grigorovici, A. Vanc, Phys. Stat. Sol. **15**, 627–637 (1966)

35. W.W. Li, J.J. Zhu, J.D. Wu, J. Gan, Z.G. Hu, M. Zhu, J.H. Chu, Appl. Phys. Lett. **97**, 121102 (2010)
36. K. Ueda, H. Yanagi, H. Hosono, H. Kawazoe, J. Phys. Condens. Matter **11**, 3535–3545 (1999)
37. E. Burstein, Phys. Rev. **93**, 632–633 (1954)
38. T.S. Moss, Proc. Phys. Soc. B **67**, 775–782 (1954)